# Temperature measurements on ES steel sheets subjected to perforation by hemispherical projectiles

J.A. Rodríguez-Martínez [a,*], A. Rusinek [b], P. Chevrier [b], R. Bernier [b], A. Arias [a]

[a] Department of Continuum Mechanics and Structural Analysis, University Carlos III of Madrid, Avda. de la Universidad 30, 28911 Leganés, Madrid, Spain
[b] National Engineering School of Metz (ENIM), Laboratory of Mechanics, Biomechanics, Polymers and Structures (LaBPS), Ile du Saulcy, 57000 Metz, France

ARTICLE INFO

ABSTRACT

In this paper is reported a study on the behaviour of **ES** mild steel sheets subjected to perforation by hemispherical projectiles. Experiments have been conducted using a pneumatic cannon within the range of impact velocities $5m/s \leq V_0 \leq 60m/s$. The experimental setup allowed evaluating initial velocity, failure mode and post mortem deflection of the plates. The tests have been recorded using high speed infrared camera. It made possible to obtain temperature contours of the specimen during impact. Thus, special attention is focussed on the thermal softening of the material which is responsible for instabilities and failure. Assuming adiabatic conditions of deformation, the increase of temperature may be related to the plastic deformation. The critical strain leading to target failure is evaluated coupling temperature measurements with numerical simulations and with analytical predictions obtained by means of the Rusinek Klepaczko constitutive relation [Rusinek, A., Klepaczko, J.R. Shear testing of sheet steel at wide range of strain rates and a constitutive relation with strain rate and temperature dependence of the flow stress. Int J Plasticity. 2001; 17, 87 115]. It has been estimated that the process of localization of plastic deformation which leads to target failure involves local values close to $\overline{\varepsilon}_f^p \approx 1$ for the boundary value problem approached. Subsequently, this failure strain level has been applied to simulate the perforation process and the numerical results obtained show satisfactory agreement with the experiments in terms of ballistic limit, temperature increase and failure mode of the target.

This paper is dedicated to **Prof. Janusz Roman Klepaczko** who passed away in August 15, 2008. We pay our tribute to him for his teaching and contribution to dynamic failure of metals. Prof. Klepaczko was involved at the beginning of this investigation.

*Keywords:*
Perforation
RK model
Infrared thermography
Dynamic failure

## 1. Introduction

The study of materials subjected to extreme loading conditions like crash, impact or explosion, has considerable interest for different industrial fields. A relevant amount of publications can be found in the international literature dealing with high strain rate behaviour of metallic materials related with different engineering applications [1 6]. During the last decades, the behaviour of metallic plates when subjected to impact by non deformable projectiles has gathered the efforts of many researchers [7 18].

Impact processes are strongly dependent on strain hardening $\theta \quad \partial\sigma/\partial\varepsilon^p$, temperature sensitivity $\upsilon \quad \partial\sigma/\partial T$ and strain rate sensitivity m $\partial\sigma/\partial\log(\dot{\varepsilon})$ of the material. Locally, plastic strain values larger than $\overline{\varepsilon}_f^p > 1$ may be reached for some metals under dynamic loading conditions [19 21]. High temperature level inducing thermal softening of the material is usually observed in such processes. It comes from an irreversible thermodynamic process which converts the plastic energy into heat. Adiabatic temperature increase is precursor of plastic instabilities and subsequent failure.

This paper is devoted to the analysis of such complex phenomena which take place during impact processes. An experimental analysis has been conducted on the impact behav iour of **ES** mild steel sheets subjected to perforation by non deformable hemispherical projectiles. Experiments have been carried out using a pneumatic cannon within the range of impact velocities $5m/s \leq V_0 \leq 60m/s$. The tests were recorded using infrared high speed camera. It allowed obtaining temperature contours during impact. Assuming adiabatic conditions of defor mation, temperature increase $\Delta T$ may be related to plastic defor mation. It makes possible to evaluate the critical failure strain $\overline{\varepsilon}_f^p$ that leads to the collapse of the target. For that task, the temperature measurements are coupled with numerical simula tions and with analytical predictions of the material behaviour obtained by means of the constitutive description due to Rusinek and Klepaczko (**RK**) [22].

* Corresponding author. Tel.: +34 91624 8809; fax: +34 91624 9430.
*E-mail address:* jarmarti@ing.uc3m.es (J.A. Rodríguez-Martínez).

## 2. Material

Mild steel **ES** has considerable relevance since it is widely used in several engineering fields as for example in automotive industry. It has been frequently studied and a significant number of works dealing with the thermo viscoplastic behaviour of this metal can be found in the literature [17,23 30]. Mild steel **ES** consists of a *ferrite pearlitic* (**BBC**) structure. The chemical composition of the mild steel **ES** (*% of weight*) is reported in Table 1.

In agreement with experimental evidences reported in [22,26] the behaviour of the steel **ES** can be considered isotropic.

## 3. Description of the experimental setup

A scheme of the sample used for the perforation tests is shown in Fig. 1. The thickness of the specimen is $h$ 1 mm and its surface is $A_t$ 140 × 140 mm$^2$. The active part of the specimen after it is screwed and clamped on the support is $A_f$ 100 × 100 mm$^2$. This configuration minimizes the potential distortions in the failure mode of the plates thanks to the boundary conditions.

Several screws symmetrically placed are used to attach the steel sheet to the clamping support, Fig. 1. It allows eliminating potential sliding effect during the tests. The mass of the hemispherical projectile used is $M_p$ 0.063 kg and its dimensions are shown in Fig. 2.

The projectiles were made of *Maragin* steel which exhibits high yield stress $\sigma_y > 1$ GPa, much higher than that corresponding to the **ES** steel under dynamic conditions of deformation, Fig. 15. In addition, the projectiles underwent a heat treatment in order to increase their hardness. A foam sabot was used in order to get the perpendicularity of the impact during the tests. It allowed launching these projectiles whose diameter was considerably smaller than the diameter of the barrel, $\phi_p < \phi_b$ 22 mm.

### 3.1. The pneumatic cannon

In order to analyze the impact behaviour of the steel sheets within the impact velocity range 5 m/s $\leq V_0 \leq$ 60 m/s, a gas cannon has been used [17,31], Fig. 3 b. This technique allows measuring the initial velocity just before the impact takes place. Such measure ment is carried out using 3 sources of light $B_i$ coupled to 3 laser diodes $C_i$ and 3 time counters. When the projectile passes through a source of light, Fig. 3 a, a time counter is trigged. This procedure is repeated 3 times defining two time intervals $\Delta t_{12}$ and $\Delta t_{23}$, Fig. 3 a. Knowing the distance between the 3 sources of light it is possible to measure two instantaneous projectile velocities $V_0^{ij}$. Their average $\overline{V}_0$ was used to define the impact velocity values reported along this document.

This experimental technique allows for an accurate definition of the ballistic limit $V_{bl}$ for the boundary value problem examined in this paper.

### 3.2. Post mortem measurement of the deflection of the targets

Post mortem measurement of the targets deflection was con ducted using a 2D profilometer, Fig. 4 a. It allowed measuring the profiles of the impacted plates with an accuracy of 3 μm ± 1 μm.

**Table 1**
Chemical composition of the mild steel **ES** (% of weight) [17,30] delivered by Arcelor-Mittal.

| Mn | Al | Cr | C | Ni | S | Cu | Si | P | N | Ti |
|---|---|---|---|---|---|---|---|---|---|---|
| 0.203 | 0.054 | 0.041 | 0.03 | 0.018 | 0.011 | 0.009 | 0.009 | 0.008 | 0.0063 | 0.002 |

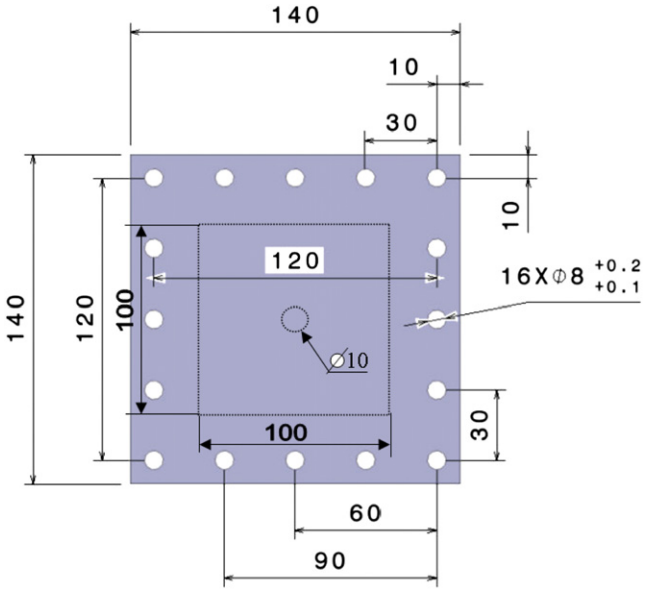


**Fig. 1.** Specimen used in the experiments.

Since measurements are carried out after impact, the displacement of the steel sheets comes exclusively from plastic deformation, Fig. 4 b. Elastic recovery cannot be taken into consideration.

Additionally, the perforation tests were recorded using a high speed infrared camera.

### 3.3. Experimental temperature measurements using infrared camera

The infrared camera used for measuring temperature contours features variable "snap shot" integration from 10 μs to 10 ms and frame rates up to 200 FPS (*Frames per Second*) in full frame mode and 6000 FPS in sub windowing mode. The minimum temperature variation registered by the camera is $\Delta T_{\min}$ 18 *mK*. The inte gration time is within the range $1\mu s \leq t_{\text{int}} \leq 20\ ms$. Such features allow having high definition and elevated frame rates. The camera was placed in different positions depending on the impact velocity. In the case of initial velocity below the ballistic limit, the camera was placed on the impact axis, on the back of the sheet steel, (*Position 1*). In the case of impact velocity above ballistic limit, the camera was placed with a small angle $\theta \approx 15^\circ$, in relation to the impact axis in order to guarantee the safety of the device, (*Position 2*) Fig. 5. The distance from the camera to the target remained approximately constant for both camera placements. During the tests it was checked that such camera angle ($\theta \approx 15^\circ$) allowed for a complete view of the rear side of the target during the impact

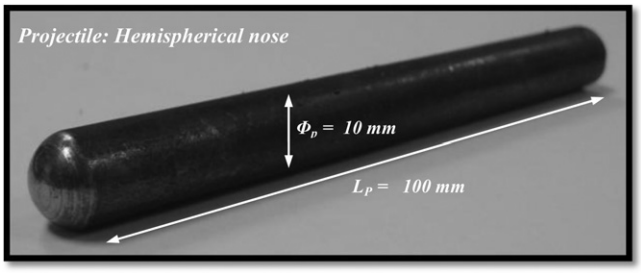


**Fig. 2.** Projectile used for perforation tests.

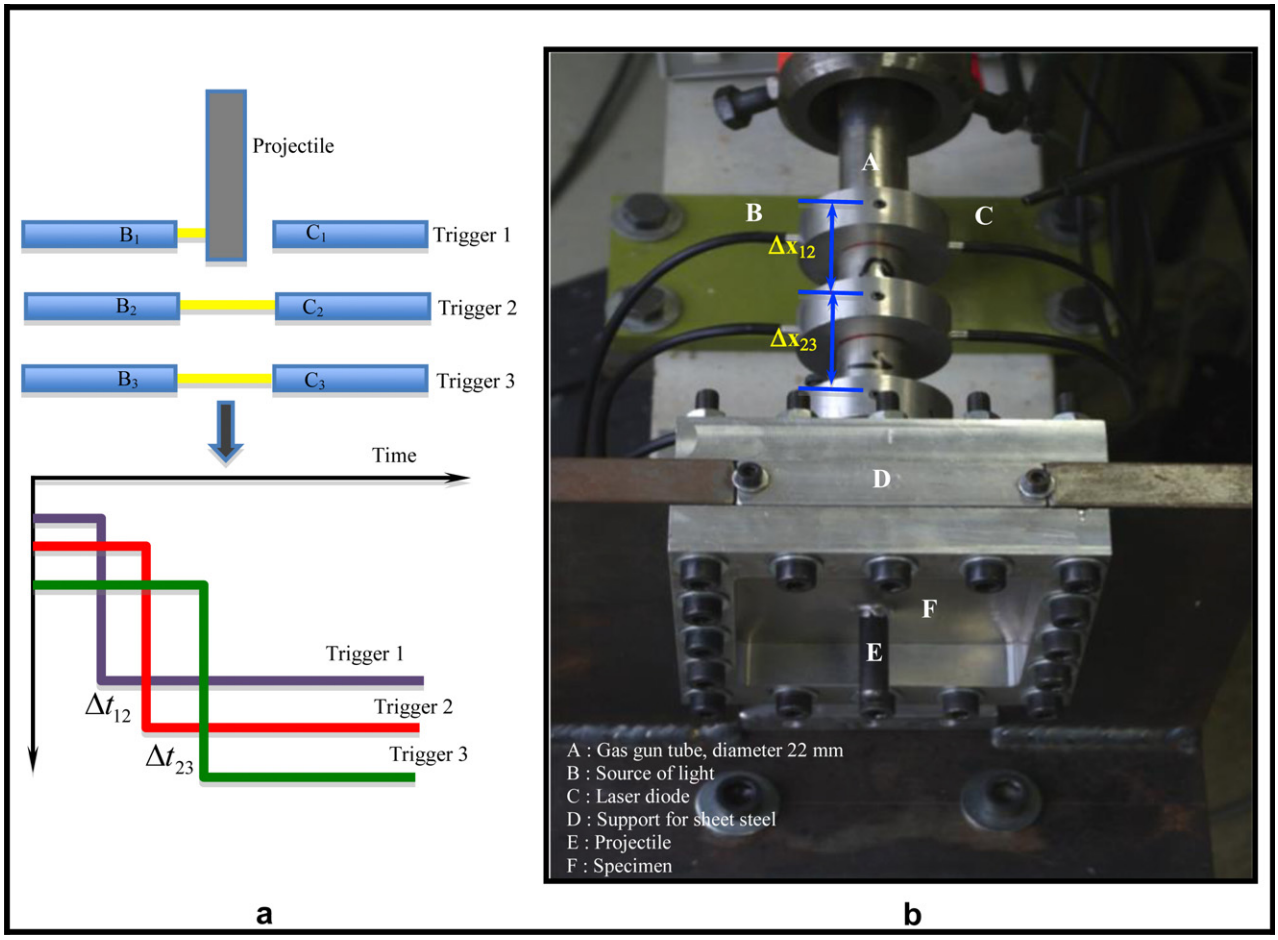


**Fig. 3.** (a) Scheme of the facility used for measurement of the impact velocity. (b) Description of the experimental setup.

process; temperature contours recorded during perforation were well defined. It is feasible to assume that the position of the camera during the tests involving perforation did not affect the tempera ture measurements.

In order to get the maximum emissivity from the target, the steel sheets were covered with soot whose emissivity was esti mated $\eta$ 0.95 (before loading, the temperature registered by the camera on the soot coated target surface must fit the room temperature) [32,33]. However, in the area surrounding the projectile impact, this coating was ejected during the high velocity tests and the emissivity was reduced to $\eta$ 0.64. This last value was obtained from the original target surface (before loading, the temperature registered by the camera on the original target surface must fit the room temperature), Fig. 6. Therefore, after recording the impact, the video images must be properly interpreted using the camera software. Suitable emissivity value is assigned to the

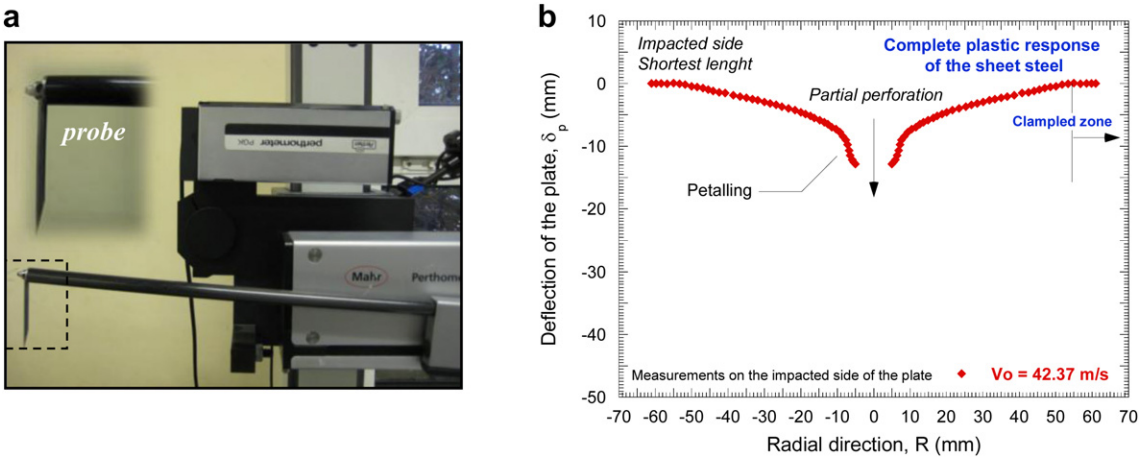


**Fig. 4.** (a) Profilometer used to measure the permanent deflection of the plates, (b) Measurement of the post-mortem deflection of the target.

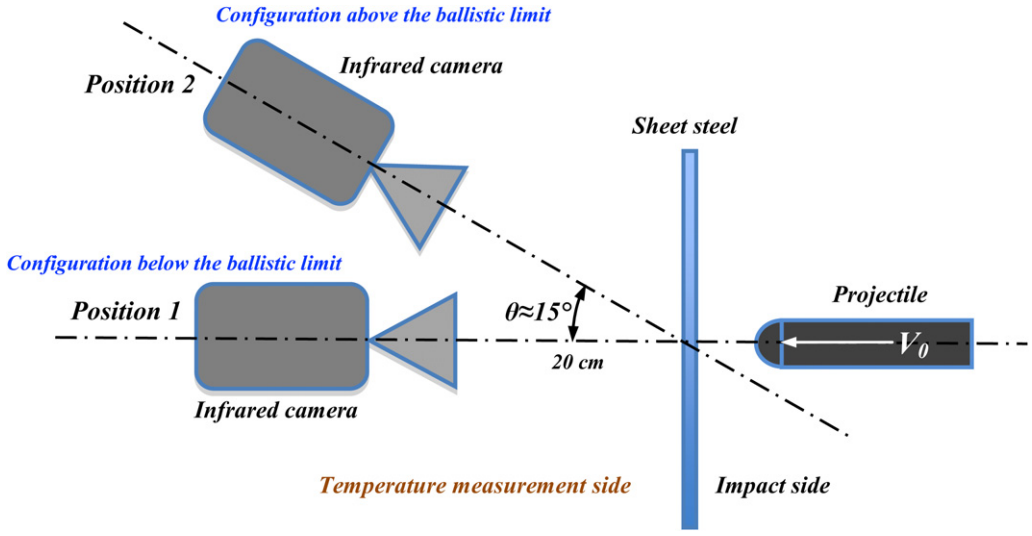


**Fig. 5.** Placements of the infrared camera during the tests depending on the impact velocity.

images depending on the target zone analyzed, Fig. 6. Assuming $\eta$ 0.64 and $\eta$ 0.95 as limiting values for the emissivity of the target during perforation, the maximum discrepancy in the temperature measurement is close to 15%.

Measurements of the temperature increase in the material target during impact $\Delta T(t)$were obtained, Figs. 7 and 8.

In view of Figs. 7 and 8, it is possible to set two well differ entiated stages during the impact. A drastic increase of tempera ture in a short period of time takes place at the beginning of loading. During this period let us assume adiabatic conditions of deformation in the target zone affected by the impact. This first stage is followed by an exponential decrease of temperature (*slower*) due to heat transfer, Figs. 7 and 8. Finally, the material reaches thermodynamic equilibrium with the surrounding temperature, Fig. 8.

The analysis of the experiments and the estimation of the crit ical failure strain inducing the target collapse are conducted along the following sections of the document.

## 4. Study of the perforation mechanisms

The ballistic limit value found from experiments is $V_{bl} \approx 45\ m/s$. In Fig. 9. are shown final stages of the impact process for different initial impact velocities. In the case of impact velocity above the ballistic limit $V_0 \approx 48\ m/s$, well developed *petalling* is observed, Fig. 9 a. A small decrease of the initial velocity, $\Delta V_0$ 6 $m/s$, strongly modifies the final stage of the impact process, Fig. 9 b. In Fig. 9 b the cracks generated at the dome of the contact projectile/ plate did not have sufficient energy to progress (*local deformation induced by the projectile in the target did not allow for crack prop agation*). Cracks were quickly arrested and the projectile was stopped before reaching complete perforation of the steel sheet. In the case of initial velocity under the ballistic limit, Fig. 9 c. it is observed a zone affected by severe plastic deformation in absence of cracks (Zone I). It corresponds to the contact projectile/sheet steel. Outside of Zone I, large permanent bending takes place (Zone II).

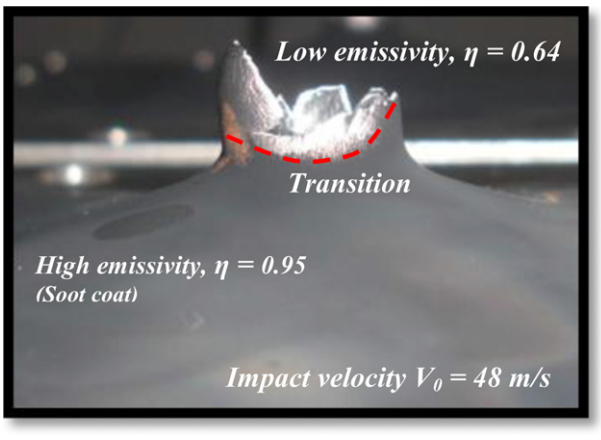


**Fig. 6.** Post-mortem estimation of the emissivity value depending on the target zone.

It has been observed a global response of the target during the perforation tests. The impact velocity range applied during the tests allows to the stress waves generated by the impact to cover the whole steel sheet before rebounding of the projectile (*in the case of impact velocity below the ballistic limit*) or perforation of the target (*in the case of impact velocity above the ballistic limit*). Deflection of the plate starts just beside the embedded perimeter, Fig. 10. Bending effect is enhanced by the small thickness of the target. Close to the ballistic limit the deflection of the plates reaches $\delta_p$ 10 mm in the zone directly affected by the impact. Large bending allows for radial sliding along the contact zone projectile/ plate leading to *necking* formation close to the dome of the contact zone projectile/plate [17]. *Necking* involves localization of defor mation acting as precursor of the onset of cracks, large plasticity values are expected in the *necking* zone [17]. When cracks are formed, they propagate radially leading to a (*approximately*) symmetric failure mode of the target.

According to the previous considerations, cracks have long distance to cover until they are arrested on the rear side of the plate. It causes formation of petals as final stage of the perforation process [17]. No plug ejection was observed during the tests (*due to formation of cracks at the dome of the contact zone projectile/ plate*).

## 5. Analysis of the temperature fields during perforation

By using infrared recording is possible to analyze localization of deformation (plastic instabilities appearance: necking formation,

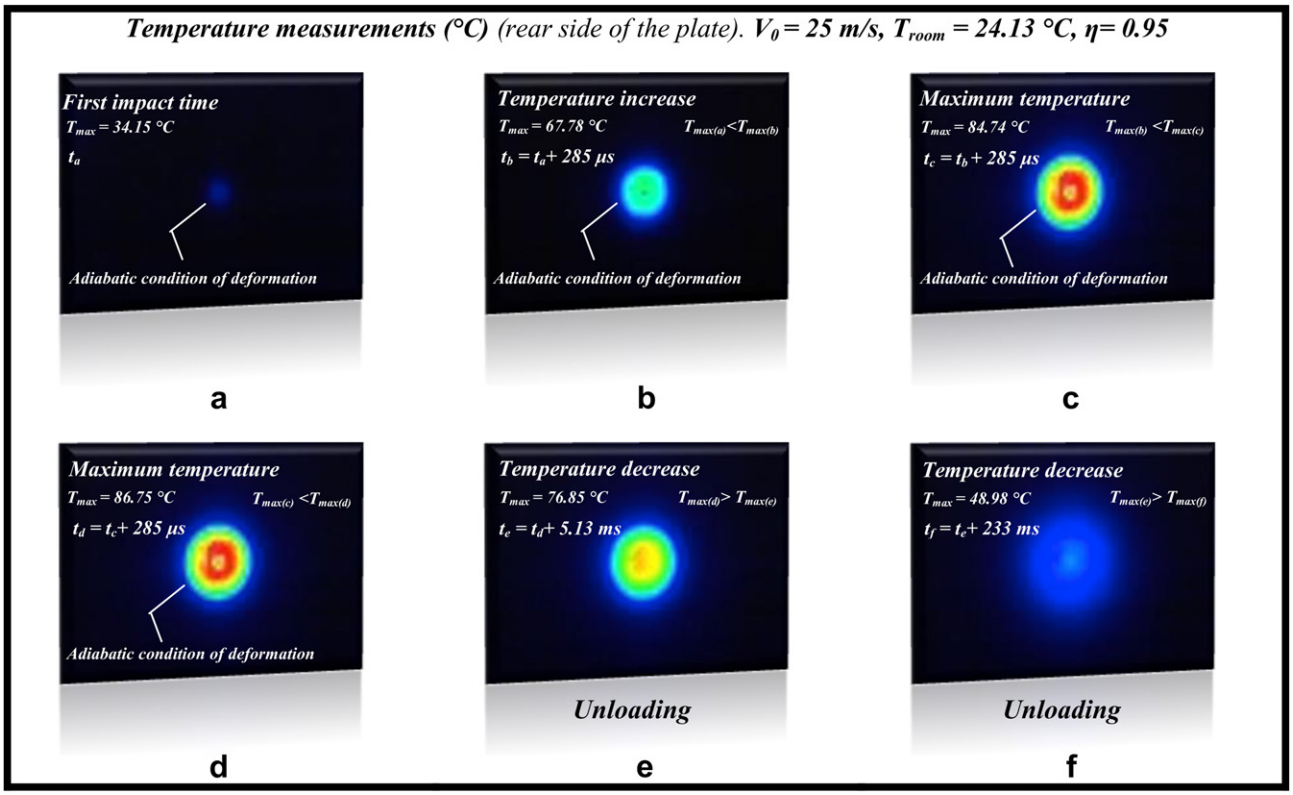


**Fig. 7.** Temperature in the rear side of the target for different stages of the impact process. $V_0$ 25 m/s and $T_{room}$ 24.13 °C. (a) $T_{max}$ 34.15 °C;(b) $T_{max}$ 67.78 °C; (c) $T_{max}$ 84.74 °C;(d) $T_{max}$ 86.75 °C; (e) $T_{max}$ 76.85 °C; (f) $T_{max}$ 48.98 °C. Picture resolution 80 × 64 pixels.

onset of cracks and their subsequent propagation) which is responsible for target failure during perforation.

In the zone directly affected by the impact, from the first contact until the onset of cracks takes place, the temperature is continuously increasing, Fig. 11. Maximum temperature increase, $\Delta T_{\max} \approx 160°C$ if $\eta$ 0.64 ($\Delta T_{\max} \approx 135°C$ if $\eta$ 0.95), corresponds to the loading time involving *necking* development and onset of cracks, Fig. 11 b c. Such temperature level strongly reduces the strain hardening of the **ES** steel [30], promoting crack propagation.

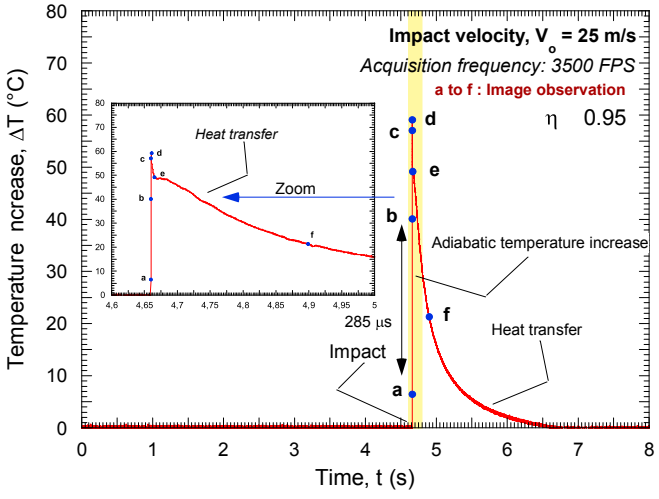


**Fig. 8.** Evolution of the maximum increase of temperature in the target as a function of time, $V_0$ 25 m/s.

Measuring the temperature level on the impact zone (*on the rear side of the plate*) the following curves are obtained for different loading times, Fig. 12 (*six stages of* Fig. 11. *correspond to six stages depicted in* Fig. 12 a b.). It can be observed that the temperature increase is not symmetrically distributed around the centre of the target, Fig. 12. Such phenomenon could be attributed to intrinsic material defects which induce certain asymmetry (*quite reduced in agreement with* Fig. 9) in the distribution of plastic deformation around the impact zone. Material defects become influential on the target failure at low impact velocities, close to the ballistic limit value. At high impact velocities (much higher than the ballistic limit and therefore out of the range of impact velocities tested in this study) initial material defects do not have time to growth due to fast failure of the target. Then it is expected that such asym metry in the temperature field will not take place. Maximum temperature level is located on the petals edge (*cracking interface*).

Away from the cracking interface, temperature increase is much more reduced, Figs. 11 and 12. In Fig. 13. is shown the temperature increase inside a circular surface centred on the impact point as a function of time. Radius of the circular surface is approximately the projectile radius. Maximum temperature level (*it corresponds to the cracking interfaces*) is much greater than the average temperature of the whole area. Strong temperature gradients take place surrounding the cracks, Figs. 12 a b, 13.

Temperature increase is found to be dependent on the impact velocity. For the whole range of impact velocities tested, as the initial velocity increases so does the maximum temperature recorded, Fig. 14 a. Moreover, in Fig. 14 a. is observed an important gap between the maximum temperature registered in the case of

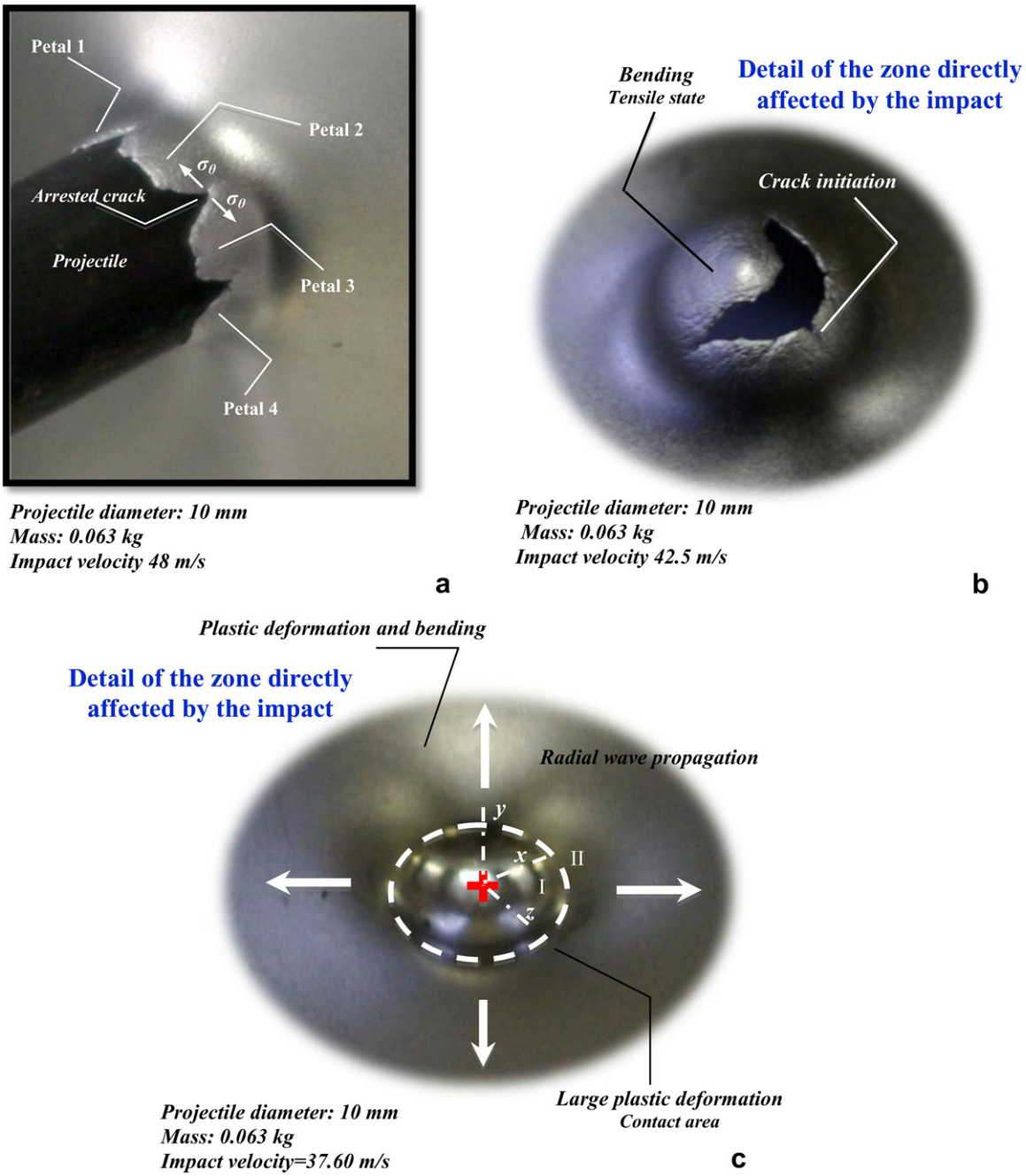


**Fig. 9.** Final stage of the impact process for initial velocities close to the ballistic limit.

impact velocity under or above the ballistic limit. In the range of $37m/s \leq V_0 \leq 42m/s$ (*in that range of impact velocities the projectile starts to pierce the target*) the slope of the curve $\Delta T_{\max}/V_0$ is maximum, Fig. 14 b. For such a range of impact velocities, small increments on the impact energy lead to large increments on the local temperature.

Previous observations may be tied to the role that deformation rate has on the material behaviour [19,34]. Therefore, in order to provide a proper interpretation of the experimental temperature dependent measurements, it is necessary to estimate the strain rate level induced in the target material by the impact. It will allow for estimation of the critical strain leading to material failure.

## 6. Estimation of the critical failure strain leading to target-failure

For this task, let us carry out the procedure described along the following sections of this paper.

### 6.1. Theoretical considerations on dissipative effects

The equation of energy balance provides the relationship between strain and temperature increase. Although it is known that potential damage mechanisms taking place during perforation generate dissipative effects [35,36], let us assume their role

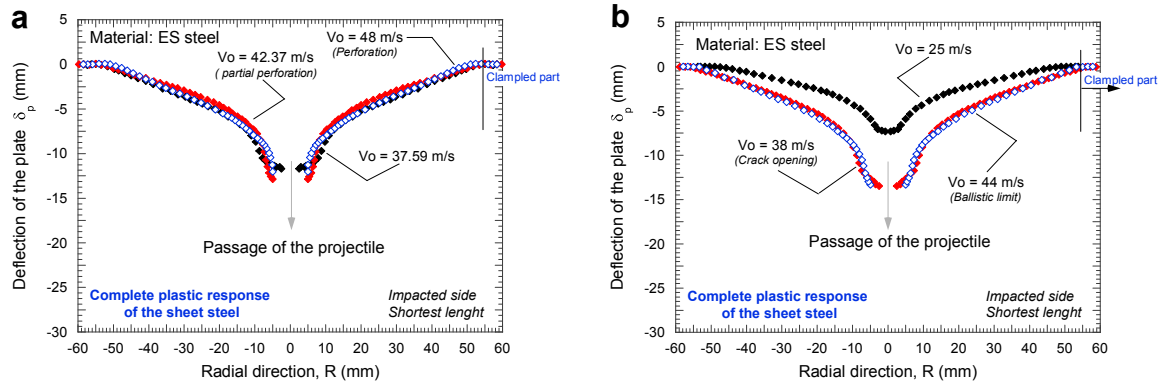


**Fig. 10.** Post-mortem deflection of the target for different initial impact velocities.

negligible in comparison with the effect due to visco plastic homogeneous flow stress.

Thus, assuming hypo elastic plastic material behaviour it is possible to set Eq. (1).

$$\lambda \cdot \nabla^2 T \quad \dot{T} \qquad \frac{\beta}{\rho \cdot C_p} \cdot \sigma_{ij} : \dot{\varepsilon}^p_{ij} + \frac{\alpha}{\rho \cdot C_p} \cdot \frac{E}{(1 \quad 2 \cdot \nu)} \cdot T \cdot tr\left(\dot{\varepsilon}^e_{ij}\right) \tag{1}$$

Where λ is the coefficient of diffusivity, T is the absolute temperature, $\dot{T}$ is the temporal temperature variation, β is the Taylor Quinney coefficient, ρ is the material density, $C_P$ is the specific heat at constant pressure, $\sigma_{ij}$ is the stress tensor, $\dot{\varepsilon}^p_{ij}$ is the plastic strain rate tensor, $\alpha$ is the coefficient of thermal expansion, E is the Young's modulus, $\nu$ is the Poisson's coefficient and $tr(\dot{\varepsilon}^e_{ij})$ is the trace of the elastic strain rate tensor.

In the plastic range, at high rate of deformation (*adiabatic conditions of deformation may be assumed when* $\dot{\bar{\varepsilon}}^p \geq 10s^{-1}$ *as reported in* [37]), the material behaves under adiabatic conditions of deformation. In such a case, the contributions to Eq. (1). due to the heat conduction and due to the elastic range can be neglected [33,36,38]. Thus, the following expression can be derived Eq. (2).

$$\dot{T} \qquad \frac{\beta}{\rho \cdot C_p} \cdot \sigma_{ij} : \dot{\varepsilon}^p_{ij} \tag{2}$$

As it was previously reported, mild steel **ES** can be assumed as an isotropic material. In such a case, by integration of the previous expression, temperature increase is defined by Eq. (3).

$$\Delta T(\bar{\varepsilon}^p, \bar{\sigma}) \qquad \frac{\beta}{\rho C_p} \int_{\varepsilon^e}^{\bar{\varepsilon}^p} \bar{\sigma}(\bar{\varepsilon}^p, \dot{\bar{\varepsilon}}^p, T) d\bar{\varepsilon}^p \tag{3}$$

Where $\bar{\sigma}(\bar{\varepsilon}^p, \dot{\bar{\varepsilon}}^p, T)$ is the equivalent stress (*considered dependent on plastic strain, strain rate and temperature*), $\bar{\varepsilon}^p$ is the current

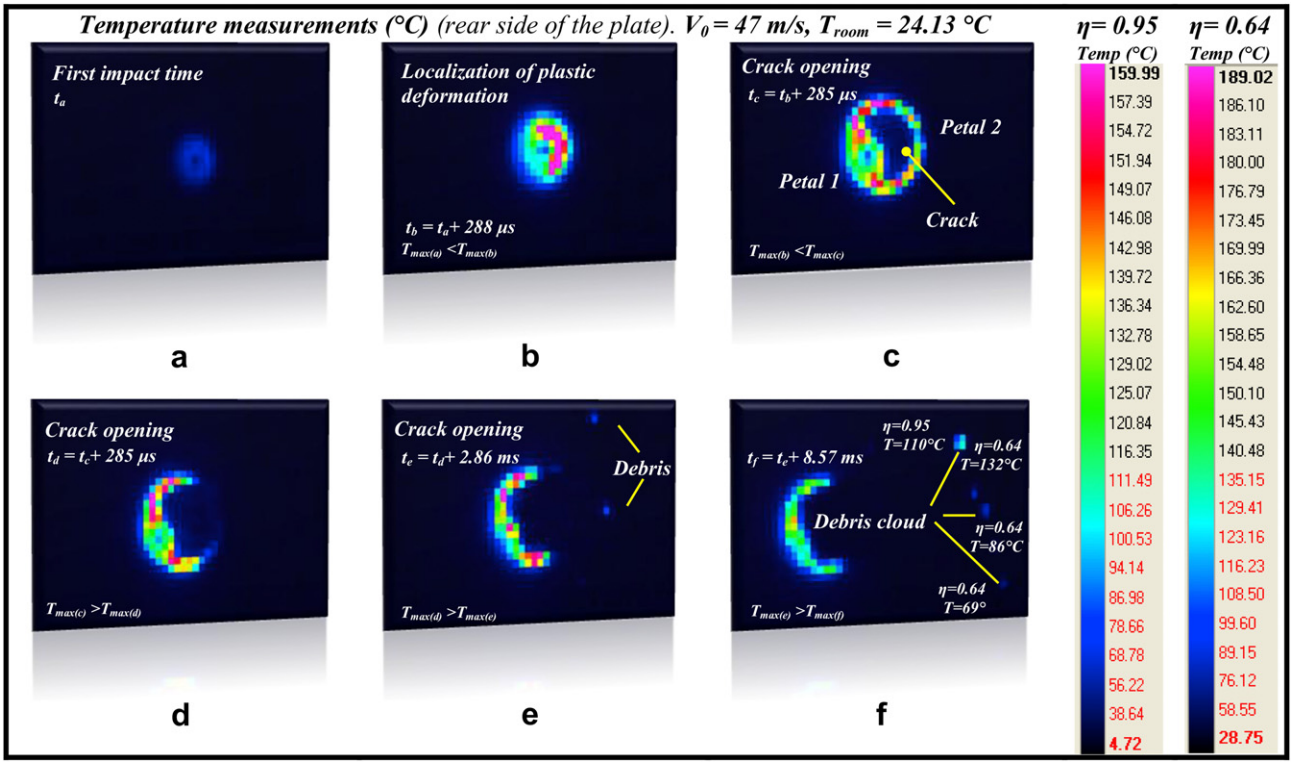


**Fig. 11.** Temperature level (°C) along the impact process for an impact velocity leading to target-perforation, observation of debris cloud during petalling formation, $V_0$ 47 m/s and $T_{room}$ 24.13 °C. Picture resolution 80 × 64 pixels.

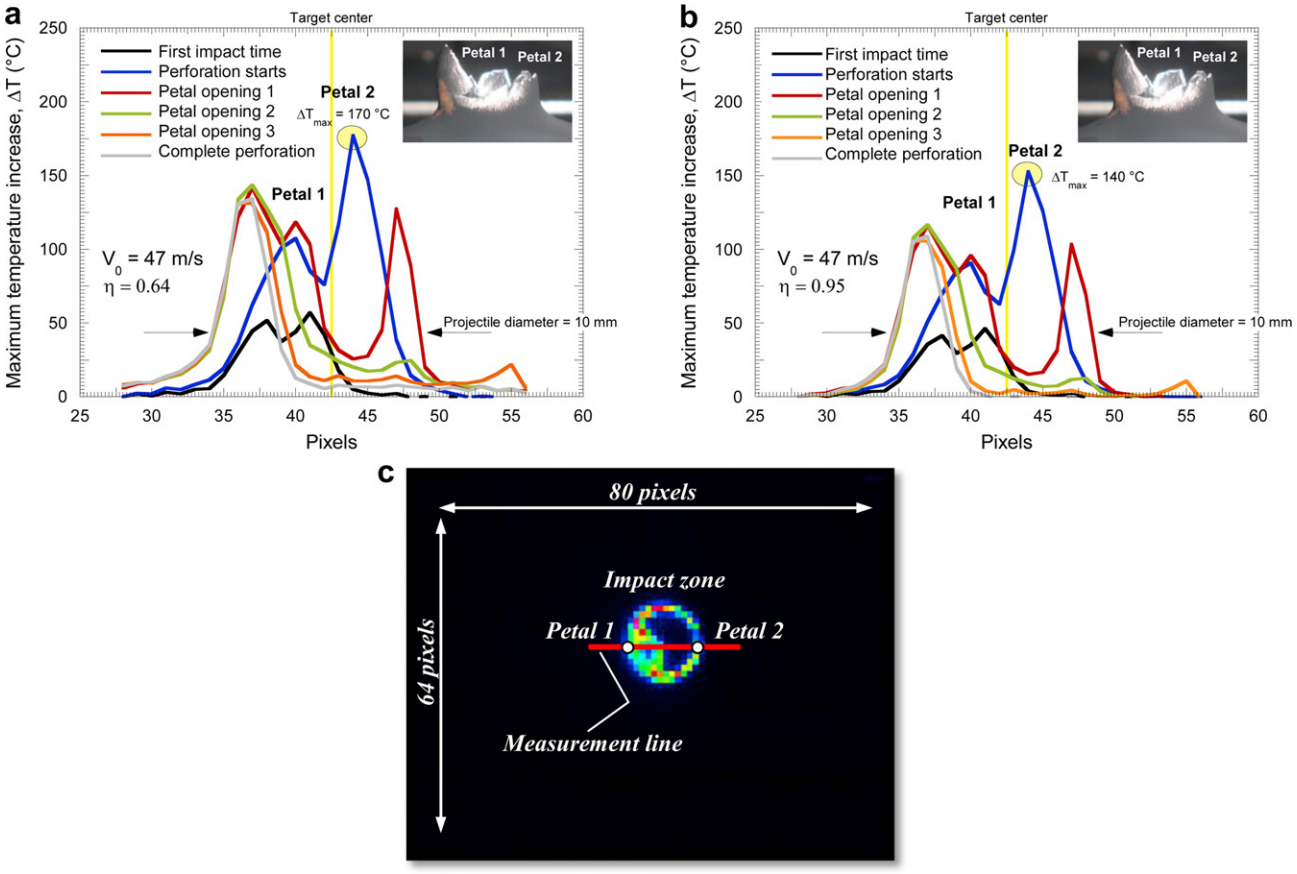


**Fig. 12.** Maximum temperature increase in the impact zone at $V_0$ 47 m/s (a) $\eta$ 0.64 and (b) $\eta$ 0.95. (c) Measurement points of the temperature increase.

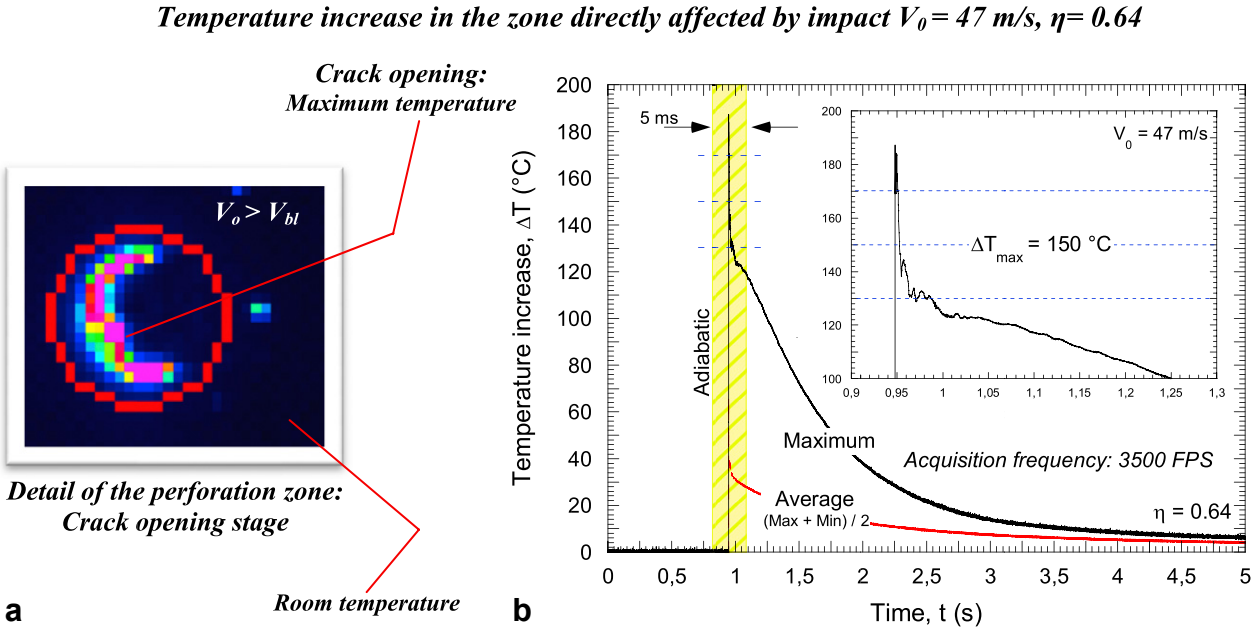


**Fig. 13.** Temperature increase corresponding to a circular surface centred on the impact zone. $V_0$ 47 m/s.

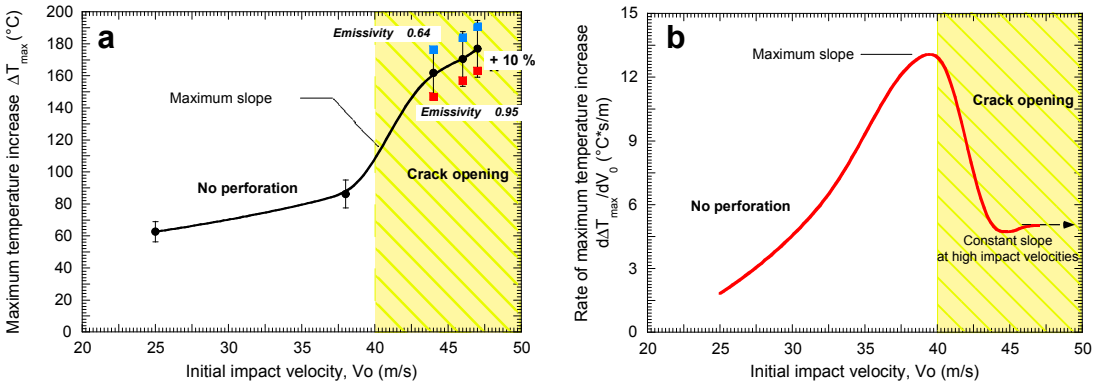


**Fig. 14.** (a) Maximum temperature increase and (b) rate of maximum temperature increase as a function of the initial impact velocity.

equivalent plastic strain, $\dot{\bar{\varepsilon}}^p$ is the equivalent plastic strain rate and $\varepsilon^e$ is the elastic strain corresponding to the initial yield stress.

Under these assumptions there is a univocal relation between temperature increase and equivalent plastic strain for an imposed deformation rate. In order to take advantage of such consideration, a proper definition of the material behaviour $\overline{\sigma}(\bar{\varepsilon}^p, \dot{\bar{\varepsilon}}^p, T)$ is necessary.

### 6.2. Modeling of the thermo viscoplastic behaviour of ES steel using RK constitutive relation and analytical description of the temperature increase

The formulation of the model [22] is based on the additive decomposition of the total stress [39 43], Eq. (4). The term acting as multiplicative factor of the stresses addition $E(T)/E_0$ defines the Young's modulus evolution with temperature [44], Eq. (5).

$$\overline{\sigma}(\bar{\varepsilon}^p, \dot{\bar{\varepsilon}}^p, T) \quad \frac{E(T)}{E_0}\left[\sigma_\mu(\bar{\varepsilon}^p, \dot{\bar{\varepsilon}}^p, T) + \sigma^*(\dot{\bar{\varepsilon}}^p, T)\right] \tag{4}$$

$$E(T) \quad E_0\left\{1 \quad \frac{T}{T_m}\exp\left[\theta^*\left(1 \quad \frac{T_m}{T}\right)\right]\right\};\ T > 0 \tag{5}$$

Where $E_0, T_m$ and $\theta^*$ denote respectively the Young's modulus at $T \quad 0$ K, the melting point and the characteristic homologous temperature. This expression allows for defining the thermal soft ening of the material depending on the crystal lattice [45]. In the case of **BBC** metals $\theta^* \approx 0.5$ and in the case of **FCC** metals $\theta^* \approx 0.9$ as reported in Rusinek at al. [45].

The athermal stress describes macroscopically the overcoming of long range barriers by mobile dislocations and it is defined by Eq. (6).

$$\overline{\sigma}_\mu(\bar{\varepsilon}^p, \dot{\bar{\varepsilon}}^p, T) \quad B(\dot{\bar{\varepsilon}}^p, T)(\varepsilon_0 + \bar{\varepsilon}^p)^{n(\dot{\bar{\varepsilon}}^p, T)} \tag{6}$$

Where the modulus of plasticity $B(\dot{\bar{\varepsilon}}^p, T)$ defines rate and temper ature sensitivities of strain hardening, $n(\dot{\bar{\varepsilon}}^p, T)$ is the strain hard ening exponent depending on strain rate and temperature and $\varepsilon_0$ is the strain level which defines the yield stress at specific strain rate and temperature.

The explicit formulations describing the modulus of plasticity and the strain hardening exponent read as follows, Eqs. (7) (8).

$$B(\dot{\bar{\varepsilon}}^p, T) \quad B_0\left(\left(\frac{T}{T_m}\right)\log\left(\frac{\dot{\varepsilon}_{\max}}{\dot{\bar{\varepsilon}}^p}\right)\right)^{-\nu} \tag{7}$$

$$n(\dot{\bar{\varepsilon}}^p, T) \quad n_0\left\langle 1 \quad D_2\left(\frac{T}{T_m}\right)\log\frac{\dot{\bar{\varepsilon}}^p}{\dot{\varepsilon}_{\min}}\right\rangle \tag{8}$$

Where $B_0$ is the material constant, $\nu$ is the temperature sensi tivity, $n_0$ is the strain hardening exponent at $T \quad 0$ K, $D_2$ is the material constant and $\dot{\varepsilon}_{\min}$ is the lower limit of the model. The McCauley operator is defined as $\langle \bullet \rangle \quad \bullet$ if $\langle \bullet \rangle \geq 0$ or $\langle \bullet \rangle \quad 0$ if $\langle \bullet \rangle \leq 0$.

The effective stress $\sigma^*(\dot{\bar{\varepsilon}}^p, T)$ is the flow stress component defining the rate dependent interactions with short range obsta cles. It denotes the rate controlling deformation mechanism from thermal activation. At temperatures $T > 0$ K, thermal activation assists the applied stress.

The theory of thermodynamics and kinetics of slip [2] is founded on a set of equations which relate activation energy $\Delta G$, mechanical threshold stress $\widehat{\sigma}$, applied stress $\overline{\sigma}$, strain rate $\dot{\bar{\varepsilon}}^p$, temperature $T$ and determined physical material parameters. Based on such understanding of the material behaviour, Rusinek and Klepaczko [22] derived the following expression, Eq. (9).

$$\sigma^*(\dot{\bar{\varepsilon}}^p, T) \quad \sigma_0^*\left\langle 1 \quad D_1\left(\frac{T}{T_m}\right)\log\left(\frac{\dot{\varepsilon}_{\max}}{\dot{\bar{\varepsilon}}^p}\right)\right\rangle^{m^*} \tag{9}$$

Where $\sigma_0^*$ is the effective stress at $T \quad 0$ K which is related to the mechanical threshold stress, $D_1$ is the material constant, $\dot{\varepsilon}_{\max}$ is the maximum strain rate accepted for a particular material and $m^*$ is the constant allowing to define the strain rate temperature dependence.

The material constants corresponding to **ES** steel are listed in Table 2.

Conventional physical constants of steel can be obtained from material handbooks, Table 3.

This model has proven capacity to describe the thermo visco plastic behaviour of the **ES** steel for wide ranges of strain rate, Fig. 15, and temperature [17,22,26,30].

**Table 2**
Constants determined for **ES** steel for **RK** model [17,26,30].

| $B_0$ (MPa) | $\nu$ (−) | $n_o$ (−) | $D_2$ (−) | $\varepsilon_0$ (−) | $\sigma_0^*$ (MPa) | $m^*$ (−) | $D_1$ (−) | $T_m$ (K) | $\dot{\varepsilon}_{\min}$ (s $^{1}$) | $\dot{\varepsilon}_{\max}$(s $^{1}$) | $\theta^*$ (−) |
|---|---|---|---|---|---|---|---|---|---|---|---|
| 591.6 | 0.2 | 0.285 | 0.19 | 0.018 | 406.3 | 2.8 | 0.48 | 1600 | $10^{5}$ | $10^{7}$ | 0.59 |

**Table 3**
Physical constants for steel alloys.

| $E_0$ (GPa) | $C_p$ (Jkg $^{1}$K $^{1}$) | $\beta$ (−) | $\rho$ (kgm $^{3}$) |
|---|---|---|---|
| 210 | 470 | 0.9 | 7800 |

Using the flow stress definition provided by the **RK** relation is possible to particularize Eq. (3). to the **ES** steel. Thus, the temper ature increase is decomposed into the contributions due to the internal stress $\sigma_\mu(\bar{\varepsilon}^p, \dot{\bar{\varepsilon}}^p, T)$ and due to the effective stress $\sigma^*(\dot{\bar{\varepsilon}}^p, T)$, Eq. (10).

$$\Delta T(\bar{\varepsilon}^p, \bar{\sigma}) \qquad \Delta T_{\text{internal stress}} + \Delta T_{\text{effective stress}} \tag{10}$$

By integration of Eq. (10), the following expression is derived, Eq. (11)

$$\Delta T(\bar{\varepsilon}^p, \bar{\sigma}) \qquad \frac{\beta}{\rho \cdot C_p} \int \frac{E(T)}{E_0} \cdot \bar{\sigma}(\bar{\varepsilon}^p, \dot{\bar{\varepsilon}}^p, T) \cdot d\bar{\varepsilon}^p$$
$$\frac{\beta}{\rho \cdot C_p} \int \frac{E(T)}{E_0} \cdot \left[\sigma_\mu(\bar{\varepsilon}^p, \dot{\bar{\varepsilon}}^p, T) + \sigma^*(\dot{\bar{\varepsilon}}^p, T)\right] \cdot d\bar{\varepsilon}^p \tag{11}$$

However, under adiabatic conditions of deformation, temperature is strain dependent $T \quad f(\bar{\varepsilon}^p)$. In the present paper, the previous expression, Eq. (11). is solved numerically in order to obtain the temperature increase. Coupling Eq. (11). with experiments and with numerical simulations an *inverse method* for estimating the failure strain of the material target during the perforation tests is proposed in the following sections of the paper.

However, it must be noticed that fracture models based on a constant strain value are a simplification for defining ductile failure. In further investigations it would be advisable to develop a methodology to gather explicitly the potential influence of the stress state and the strain rate on the definition of the critical strain under dynamic loading.

### *6.3. Finite element simulation of the impact process in order to estimate the strain rate level induced on the material during perforation*

Once it is possible to obtain the temperature increase depending on strain (*for an imposed deformation rate*) using Eq. (11)., it is necessary to get an estimation of the strain rate level in the target material during perforation.

For that task, numerical simulations of the perforation process have been conducted using the **FE** code **ABAQUS/Explicit**. The **RK** constitutive relation has been implemented into the code using the implicit consistent algorithm proposed by Zaera and Fernández Sáez [46].

According to the observations which are reported in [17], the numerical simulations have been conducted using a fully **3D** description of the problem. The mesh used for the target is shown in Fig. 16. It presents radial symmetry to avoid appearance of spurious generation of cracks. The zone directly affected by the impact has been meshed with 222,400 8 node tri linear elements with reduced integration (**C3D8R** in **ABAQUS** notation). In this zone ten elements are placed along the thickness. In order to reduce the computational time, beyond the zone directly affected by the impact is defined a transition zone using 50,413 tetrahedral elements. This technique allows decreasing the number of elements along the thickness of the plate. In this transition zone the amount of elements along thickness is varied from ten to two. After the transition zone, the mesh is defined using **C3D8R** elements until getting the perimeter of the target. This optimum configura tion has been obtained from a convergence study using different mesh densities.

Since the experimental observations revealed absence of erosion on the projectile surface after the impact (*the projectile was not deformed plastically in any test*), the projectile has been defined as rigid body, Fig. 16. It enables to reduce the computa tional time required for the simulations. A constant friction

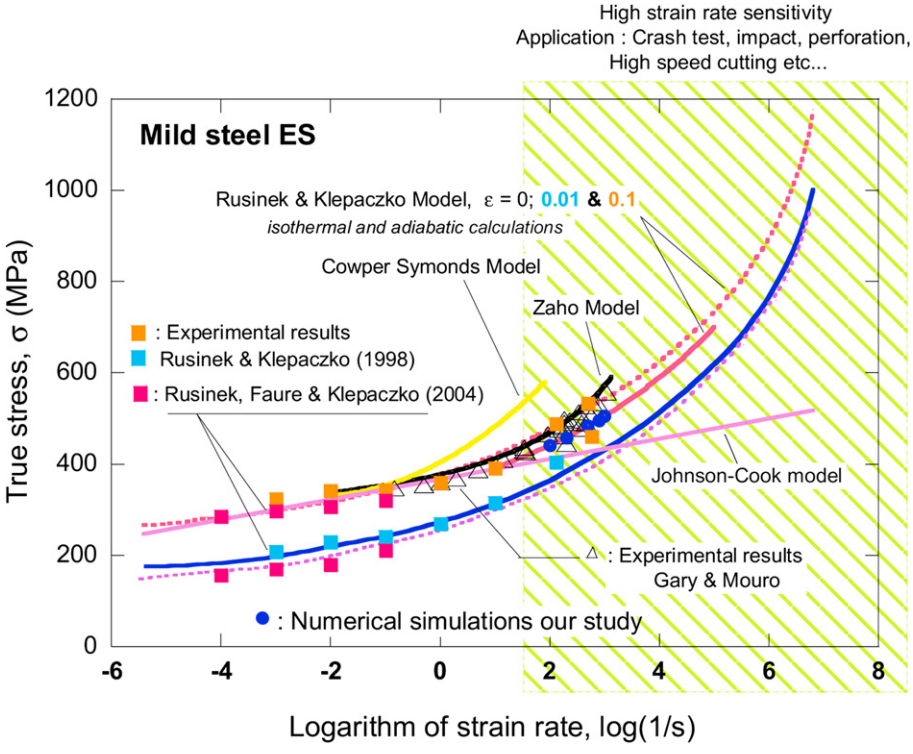


**Fig. 15.** Analytical predictions of ES steel behaviour using RK model and comparison with experiments within the strain rate range $10^{4} s^{1} \leq \dot{\bar{\varepsilon}}^p \leq 5\ 10^{3} s^{1}$.

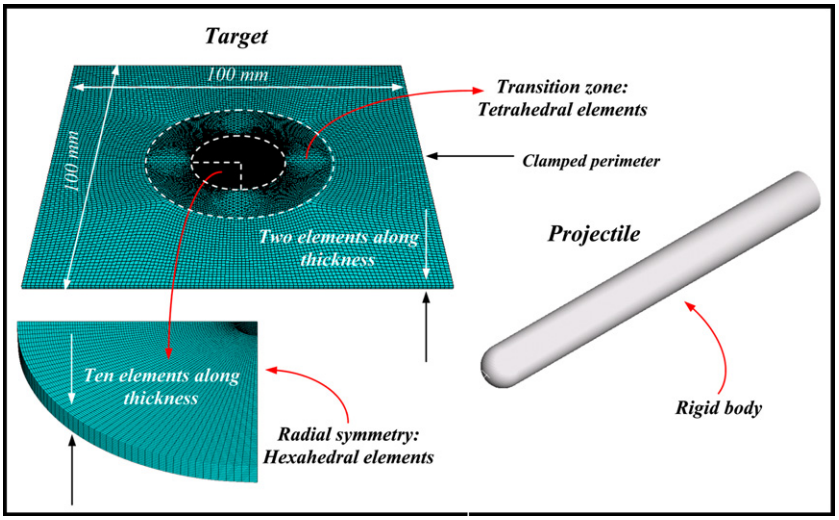


**Fig. 16.** Numerical configuration used in the simulations.

coefficient value $\mu$ 0.1 has been used to define the contact projectile/plate [16].

The impact velocities covered with the numerical simulations are those covered during the experiments.

The procedure for obtaining the strain rate level is the following:

Maximum material deformation allowed during the simulations is $\bar{\varepsilon}^p$ 1.5. Let us assume that during the experiments the local strain is lower than that value (*such assumption will be verified in the next section of the document when analytical predictions and experiments will be compared*).

As soon as deformation reaches $\bar{\varepsilon}^p$ 1.5 in one integration point, the simulation is stopped (It could be automatically stopped before reaching such a condition if the elements distortion becomes excessive).

Finally, the strain rate contours predicted by the simulations are analyzed along loading time.

In Figs. 17 and 18. are shown deformation rate fields for two initial velocities ($V_0$ *25 m/s and* $V_0$ *50 m/s*) and different stages of the impact process. They correspond approximately to the maximum and to the minimum of the impact velocities covered during the experiments. Maximum strain rate values are located along the contact zone projectile/target, where localization of deformation takes place (*In Figs. 17 and 18. it is visible the onset of necking precursor of failure*). For all the loading conditions shown in Figs. 17 and 18. the maximum strain rate level is varying within the range $10^3 s^{-1} \leq \dot{\bar{\varepsilon}}^p < 10^4 s^{-1}$. Such values are within the range of strain rates where the **RK** model defines properly the behaviour of the **ES** steel as previously reported in Fig. 15.

Thus, let us assume that range of strain rate $10^3 s^{-1} \leq \dot{\bar{\varepsilon}}^p < 10^4 s^{-1}$ for coupling the experimental temperature measurements with the analytical predictions of the **RK** model. It will allow for estimation of a lower and an upper limit of the critical failure strain of the material during the perforation tests.

### 6.4. Coupling of experimental temperature measurements with analytical predictions of RK model and results obtained from numerical simulations

In Fig. 19. is depicted the temperature increase predicted by the **RK** model Eq. (11). versus plastic strain for different strain rates Fig. 19 a, and versus strain rate for different deformation levels Fig. 19 b. Let us tie the maximum temperature measured during experiments $\Delta T_{\max} \approx 150°C$ (*which corresponds to target failure condition using* $\eta$ 0.64 *as it was previously reported*) to the critical failure strain, $\bar{\varepsilon}^p_f$. To obtain such a value of temperature $\Delta T_{\max} \approx 150°C$ for the range of strain rates estimated

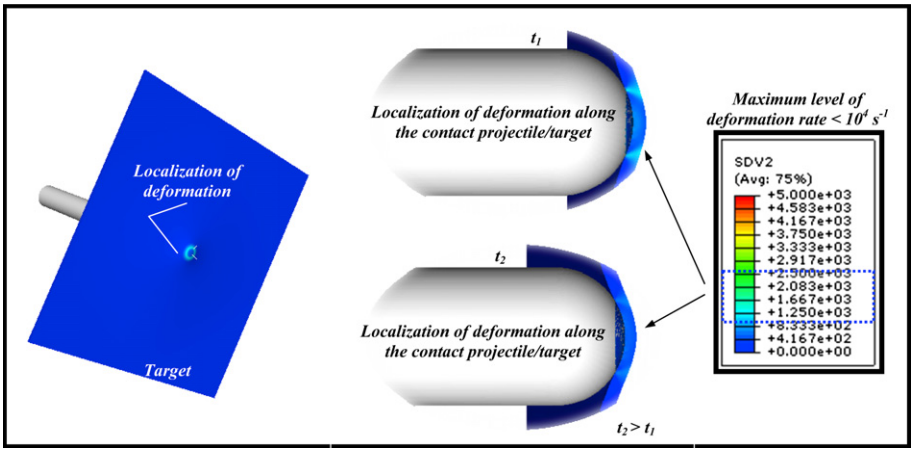


**Fig. 17.** Numerical estimations of strain rate contours during perforation, $V_0$ 25 m/s.

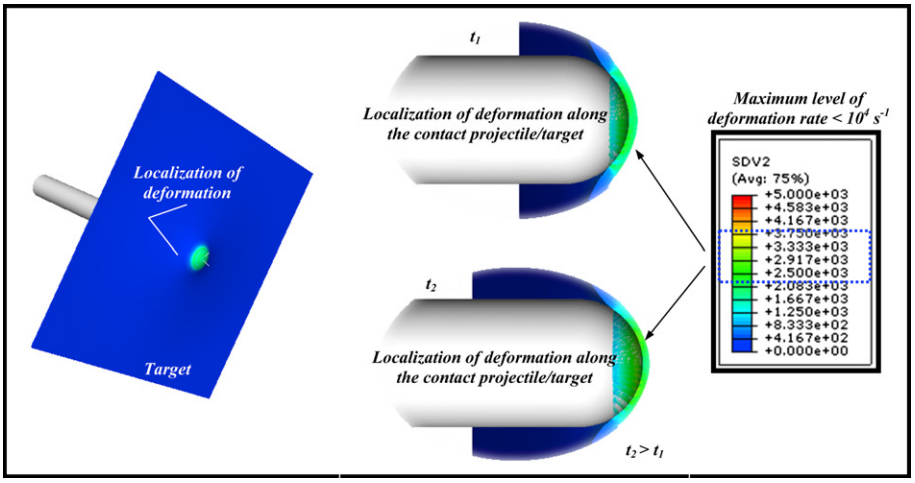


**Fig. 18.** Numerical estimations of strain rate contours during perforation, $V_0$ 50 m/s.

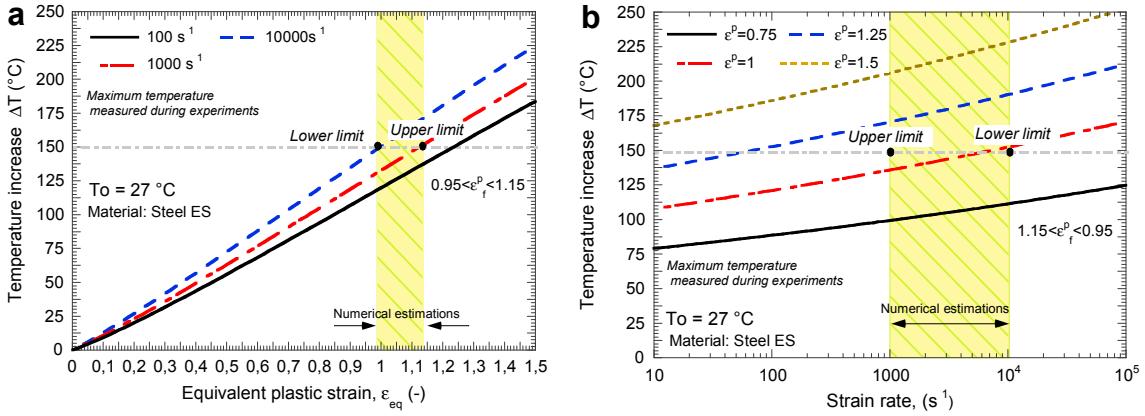


**Fig. 19.** Analytical predictions of the RK model for the temperature increase in ES steel. (a) Temperature increase as a function of plastic deformation, (b) temperature increase as a function of strain rate.

$(10^3 s^{-1} \leq \dot{\bar{\varepsilon}}^p < 10^4 s^{-1})$ it is necessary at least $\bar{\varepsilon}^p$ 0.95 in the case of $\dot{\bar{\varepsilon}}^p$ $10^3 s^{-1}$ or $\bar{\varepsilon}^p$ 1.15 in the case of $\dot{\bar{\varepsilon}}^p$ $10^3 s^{-1}$, Fig. 19. This range for the critical failure strain $0.95 \leq \bar{\varepsilon}^p_f \leq 1.15$ (*values consid erably lower than that used to estimate the strain rate level during perforation,* $\bar{\varepsilon}^p_f$ 1.5) is in agreement with experimental results and analytical predictions reported for steels for example in [20,21,29,47].

Numerical simulations of the impact process are conducted using the critical failure strain previously estimated. Next, they are compared with experiments.

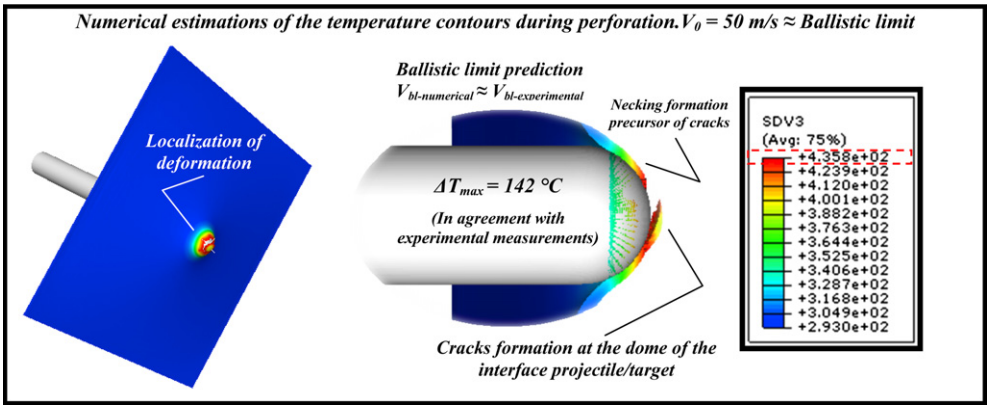


**Fig. 20.** Numerical estimations of temperature contours during perforation, $V_0$ 50 m/s.

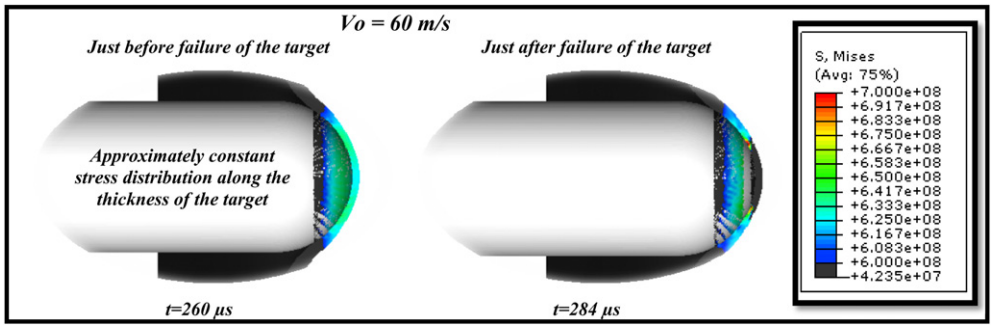


**Fig. 21.** Numerical estimation of stress contours during perforation. Vo 60 m/s.

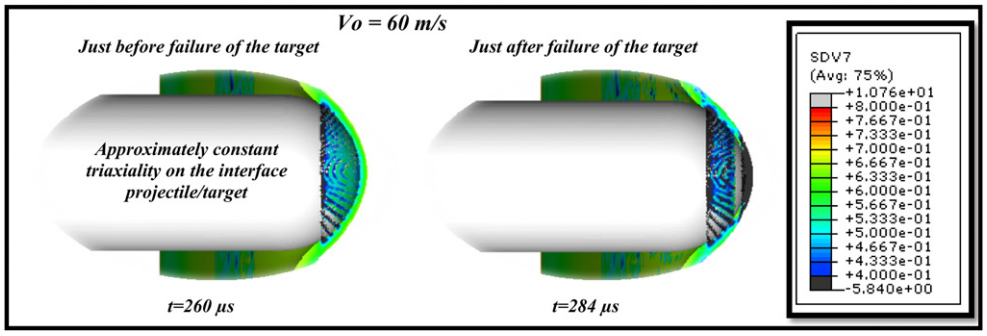


**Fig. 22.** Numerical estimation of triaxiality contours during perforation. Vo 60 m/s.

### 6.5. Comparison between experiments and numerical simulation

Numerical simulations of the perforation process using $\bar{\varepsilon}_f^p$ 1 (*average value of those obtained previously*) as failure criterion (*erosive failure criterion involving element deletion*) are conducted. In Fig. 20. it is observed that the numerical estimation of the ballistic limit matches with that obtained from experiments ($V_{\text{bl-numerical}} \approx V_{\text{bl-experimental}} \approx 50$ m/s). In addition, the numerical prediction of the failure mode of the specimen fits properly the experimental observations, Fig. 20. Radial cracks take place at the dome of the interface projectile/target, Fig. 20. Petalling development and large bending effect are in agreement with Fig. 9. Finally, it must be noted that the maximum temperature increase registered during the simulations agrees with the experimental temperature measure ments reported in previous sections of this paper, Fig. 20.

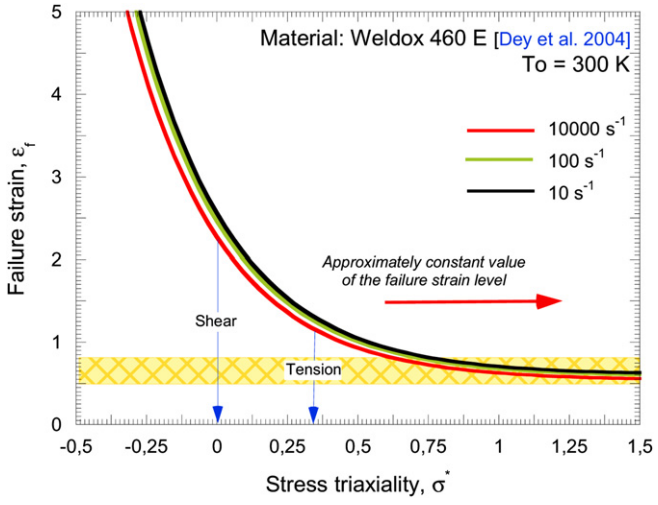


**Fig. 23.** Estimation of the failure strain versus triaxiality by the Johnson-Cook failure criterion for Weldox 460-E ferritic steel [48].

It must be noticed that this simplified estimation of the failure strain allows obtaining numerical results in agreement with experiments due to the particularities of the of the boundary value problem approached. Since the target is very thin, the stress field along the thickness of the plate is rather constant during the perforation process (*plane stress state*), Fig. 21.

Moreover, failure of the target is due to ductile hole enlargement and subsequent necking which involves stress triaxiality values $\sigma^* \geq 1/2$, Fig. 22.

For ductile metals, within that range of stress states, the failure strain becomes rather independent of triaxiality as reported in [48], Fig. 23.

Thus, following an *inverse methodology* of analysis an estimation of the critical strain leading to material failure during the perfora tion tests has been derived. In addition, the procedure followed in this study shows the role played by the local phenomena that, in impact problems, lead to plastic instabilities formation and subse quent material failure.

## 7. Concluding and remarks

In this paper is examined the perforation process of **ES** steel sheets subjected to perpendicular impact by hemispherical projectiles. The experiments have been conducted using a gas gun within the range of impact velocities $5\ m/s \leq V_0 \leq 60\ m/s$. The experimental setup allowed measuring initial velocity, failure mode and post mortem deflection of the plates. Moreover, the tests have been recorded using high speed infrared camera. Such arrangement allowed obtaining the temperature contours of the target material during perforation. Assuming adiabatic conditions of deformation along the contact interface projectile/plate, the increase of temperature is related to the plastic deformation. The critical failure strain leading to target collapse is evaluated coupling temperature measurements with numerical simulations and with analytical predictions of the material behaviour obtained by means of the Rusinek Klepaczko model. Following such procedure it has

been estimated that the process of localization of deformation which is precursor of target failure involves local plasticity values close $\varepsilon_f^p \approx 1$. The application of such value of failure strain to numerical simulations of the perforation tests provides results in agreement with experiments.

In further studies, the dissipative effects of the damage mechanics should be taken into account in the heat generation. It would allow for a more accurate evaluation of the mechanisms involved in the temperature increase of the material during perforation. In addition, it would be advisable to develop a meth odology to gather explicitly the potential influence of the stress state and the strain rate on the definition of the critical strain under dynamic loading. Such improvements would allow us to go further on the comprehension of the mechanisms responsible for ductile failure under rate dependent loading events.

## Acknowledgements

The authors express their thanks Dr. Edgar Dossou from LPMM for his technical support.

The authors would like to thank M. Patrice Balcon from FLIR Company to provide the camera for infrared measurements and for his valuable advices during experiments performance.

The researchers of the University Carlos III of Madrid are indebted to the Comunidad Autónoma de Madrid (Project CCG08 UC3M/MAT 4464) and to the Ministerio de Ciencia e Innovación de España (Project DPI/2008 06408) for the financial support received which allowed conducting the numerical simulations of this work.

## References

[1] Klepaczko JR. Generalized conditions for stability in tension test. Int J Mech Sci 1968;10:297.
[2] Kocks UF, Argon AS, Ashby MF. Thermodynamics and kinetics of slip. In: Chalmers B, Christian JW, Massalski TB, editors. Progress in materials science, vol. 19. Oxford: Pergamon Press; 1975.
[3] Follansbee P.S. High-strain-rate deformation of FCC metals and alloys. Metallurgical applications of shock-wave and high-strain-rate phenomena 1986:451–79.
[4] Zerilli FJ, Armstrong RW. The effect of dislocation drag on the stress-strain behaviour of FCC metals. Acta Metall Mater 1992;40(8):1803–8.
[5] Nemat-Nasser S, Li Y. Flow stress of FCC polycrystals with application to OFHC Copper. Acta Mater 1998;46:565–77.
[6] Nemat-Nasser S, Guo WG. Thermomechanical response of DH-36 structural steel over a wide range of strain rates and temperatures. Mech Mat 2003;35:1023–47.
[7] Taylor GI. The formation of enlargement of circular holes in thin plastic plates. Q J Mech Appl Math 1948;1:103–24.
[8] Paul B, Zaid M. Normal perforation of a thin plate by truncated projectiles. J Franklin Inst 1957;264:117–26.
[9] Zaid M, Paul B. Mechanics of high speed projectile perforation. J Franklin Inst 1958;265:317–35.
[10] Landkof B, Goldsmith W. Petalling of thin, metallic plates during penetration by cylindro-conical projectiles. Int J Solids Struct 1993;21:245–66.
[11] Wierzbicki T. Petalling of plates under explosive and impact loading. Int J Impact Eng 1999;22:935–54.
[12] Borvik T, Langseth M, Hoperstad OS, Malo KA. Perforation of 12 mm thick steel plates by 20 mm diameter projectiles with flat, hemispherical and conical noses Part I: experimental study. Int J Impact Eng 2002;27(1):19–35.
[13] Borvik T, Langseth M, Hoperstad OS, Malo KA. Perforation of 12 mm thick steel plates by 20 mm diameter projectiles with flat, hemispherical and conical noses Part II: numerical study. Int J Impact Eng 2002;27(1):37–64.
[14] Gupta NK, Iqbal MA, Sekhon GS. Effect of projectile nose shape, impact velocity and target thickness on deformation behaviour of aluminium plates. Int J Solids Struct 2007;44(10):3411–39.
[15] Arias A, Rodríguez-Martínez JA, Rusinek A. Numerical simulations of impact behaviour of thin steel to cylindrical, conical and hemispherical non-deformable projectiles. Eng Fract Mech 2008;75:1635–56.
[16] Rusinek A, Rodríguez-Martínez JA, Arias A, Klepaczko JR, López-Puente J. Influence of conical projectile diameter on perpendicular impact of thin steel plate. Eng Fract Mech 2008;75:2946–67.
[17] Rusinek A, Rodríguez-Martínez JA, Zaera R, Klepaczko JR, Arias A, Sauvelet C. Experimental and numerical analysis of failure process of mild steel sheets subjected to perpendicular impact by hemispherical projectiles. Int J Impact Eng 2009;36:565–87.
[18] Klepaczko JR, Rusinek A, Rodríguez-Martínez JA, Pecherski RB, Arias A. Modeling of thermo-viscoplastic behaviour of DH-36 and Weldox 460-E structural steels at wide ranges of strain rates and temperatures, comparison of constitutive relations for impact problems. Mech Mater 2009;41:599–621.
[19] Hu X, Daehn GS. Effect of velocity on flow localization in tension. Acta Mater 1996;44:1021–33.
[20] Pandolfi A, Krysl P, Ortiz M. Finite element simulation of ring expansion and fragmentation. Int J Fract 1999;95:279–97.
[21] Triantafyllidis N, Waldenmyer JR. Onset of necking in electro-magnetically formed rings. J Mech Phys Solids 2004;52:2127–48.
[22] Rusinek A, Klepaczko JR. Shear testing of sheet steel at wide range of strain rates and a constitutive relation with strain-rate and temperature dependence of the flow stress. Int J Plasticity 2001;17:87–115.
[23] Zhao H, Gary G. The testing and behaviour modelling of sheet metals at strain rates from 10_4 to 104 s_1. Mater Sci Eng 1996;207:46–50.
[24] Klepaczko JR, Viem Nguyen H, Nowacki WK. Quasi-static and dynamic shearing of sheet metals. Eur J Mech 1999;18:271–89.
[25] Mouro P, Gary G, Zhao H. Dynamic tensile testing of sheet metal. J Phys IV 2000;10:149–54.
[26] Rusinek A, Zaera R, Klepaczko JR, Cheriguene R. Analysis of inertia and scale effects on dynamic neck formation during tension of sheet steel. Acta Mater 2005;53:5387–400.
[27] Larour P, Baumer A, Bleck W. High strain rate tensile testing of modern car body steels. In: SCT05 conference proceeding, Wiesbaden, Germany; 2005. pp. 1–8.
[28] Haugou G, Markiewicz E, Fabis J. On use of the non direct tensile loading on a classical split Hopkinson bar apparatus dedicated to sheet metal specimen characterisation. Int J Impact Eng 2006;32:778–98.
[29] Rusinek A, Zaera R. Finite element simulation of steel ring fragmentation under radial expansion. Int J Impact Eng 2007;34:799–822.
[30] Rusinek A, Zaera R, Klepaczko JR. Constitutive relations in 3-D for a wide range of strain rates and temperatures – application to mild steels. Int J Solids Struct 2007;44:5611–34.
[31] Segreti M, Rusinek A, Klepaczko JR. Experimental study on puncture of PMMA at low and high velocities, effect on the failure mode. Polym Test 2004;23:703–18.
[32] Guzmán R, Essa YE, Meléndez J, Aranda J, López F, Pérez-Castellanos JL. Measurement of temperature increment in compressive quasi-static and dynamic tests using the infrared thermography. Strain 2008;. doi:10.1111/j.1475-1305.2007.00384x.
[33] Guzmán R, Meléndez, Zahr J, Pérez-Castellanos. Determination of the constitutive relation parameters of a metallic material by measurement of temperature increment in compressive dynamic tests. Exp Mech. doi:10.1007/s11340-009-9223-z.
[34] Altynova M, Hu X, Daehn GS. Increased ductility in high velocity electromagnetic ring expansion. Metall Trans A 1996;27:1837–44.
[35] Abu Al-Rub RK, Voyiadjis GZ. A finite strain plastic-damage model for high velocity impact using combined viscosity and gradient localization limiters: part I – theoretical formulation. Int J Damage Mech 2006;15:293–334.
[36] Perzyna P. Application of the thermodynamical theory of elasto–viscoplasticity in modern manufacturing processes. Course notes: damage mechanics and micromechanics of localized fracture phenomena in inelastic solids. Udine: CISM; July 7–11, 2008.
[37] Oussouaddi O, Klepaczko JR. Analysis of transition between the isothermal and adiabatic deformation in the case of torsion of a tube. J de Physique IV 1991;1:323–34 [in French].
[38] Klepaczko JR. Review on critical impact velocities in tension and shear. Int J Impact Eng 2005;32:188–209.
[39] Seeger A. The mechanism of glide and work-hardening in facecentered cubic and hexagonal close-packed metal. In: Dislocations and mechanical properties of crystals. New York: J. Wiley; 1957.
[40] Klepaczko JR. Thermally activated flow and strain rate history effects for some polycrystalline FCC metals. Mater Sci Eng 1975;18:121–35.
[41] Zerilli FJ, Armstrong RW. Dislocation-mechanics-based constitutive relations for material dynamics calculations. J Appl Phys 1987;1987(61):1816–25.
[42] Abed FH, Voyiadjis GZ. Plastic deformation modeling of AL-6XN stainless steel at low and high strain rates and temperatures using a combination of bcc and fcc mechanisms of metals. Int J Plast 2005;21:1618–39.
[43] Rodríguez-Martínez JA, Rusinek A, Klepaczko JR. Constitutive relation for steels approximating quasi-static and intermediate strain rates at large deformations. Mech Res Comm 2009;36:419–27.
[44] Klepaczko J.R. A general approach to rate sensitivity and constitutive modeling of FCC and BCC metals, in: Impact: effects of fast transient loadings. Rotterdam 1998:3–35.
[45] Rusinek A, Rodriguez-Martinez JA, Klepaczko JR, Pecherski RB. Analysis of thermo-visco-plastic behaviour of six high strength steels. J Mater Des 2009;30:1748–61.
[46] Zaera R, Fernández-Sáez J. An implicit consistent algorithm for the integration of thermoviscoplastic constitutive equations in adiabatic conditions and finite deformations. Int J Solids Struc 2006;43:1594–612.
[47] Borvik T, Langseth M, Hopperstad OS, Malo KA. Ballistic penetration of steel plates. Int J Impact Eng 1999;22:855–86.
[48] Dey S, Børvik T, Hopperstad OS, Leinum JR, Langseth M. The effect of target strength on the perforation of steel plates using three different projectile nose shapes. Int J Impact Eng 2004;8-9:1005–38.